Layer- and strain-dependent optoelectronic properties of hexagonal AlN

D. Kecik,[1] C. Bacaksiz,[2] R. T. Senger,[2] and E. Durgun[1,3,*]

[1]*UNAM-National Nanotechnology Research Center, Bilkent University, Ankara 06800, Turkey*
[2]*Department of Physics, Izmir Institute of Technology, 35430 Izmir, Turkey*
[3]*Institute of Materials Science and Nanotechnology, Bilkent University, Ankara 06800, Turkey*

Motivated by the recent synthesis of layered hexagonal aluminum nitride (*h*-AlN), we investigate its layer- and strain-dependent electronic and optical properties by using first-principles methods. Monolayer *h*-AlN is a wide-gap semiconductor, which makes it interesting especially for usage in optoelectronic applications. The optical spectra of 1-, 2-, 3-, and 4-layered *h*-AlN indicate that the prominent absorption takes place outside the visible-light regime. Within the ultraviolet range, absorption intensities increase with the number of layers, approaching the bulk case. On the other hand, the applied tensile strain gradually redshifts the optical spectra. The many-body effects lead to a blueshift of the optical spectra, while exciton binding is also observed for 2D *h*-AlN. The possibility of tuning the optoelectronic properties via thickness and/or strain opens doors to novel technological applications of this promising material.

PACS number(s): 81.05.ue, 78.67.−n, 68.65.−k

I. INTRODUCTION

Intensive research efforts following the discovery of monolayer graphene and its unique properties [1] have led to the emergence of novel ultrathin two-dimensional (2D) structures such as hexagonal boron nitride (*h*-BN) and transition metal dichalcogenides (TMDs). One of the main reasons for the growing interest in such materials is their optical properties. It was shown that graphene reflects only 0.1% of the incident light in the visible region [2], which can be enhanced by increasing the number of layers [3]. It was also demonstrated that graphene flakes can be made luminescent by mild oxygen plasma treatment [4]. In addition, Mak *et al.* reported that distinct optical conductivity spectra were observed for different samples having the same number of layers. The effect of stacking order on the electronic structure of few-layer graphene was also shown [5]. Lui *et al.* experimentally demonstrated a waveguide-integrated electroabsorption modulator, based on monolayer graphene with broadband and high speed. Owing to the high modulation efficiency of graphene, the device has 25 μm^2 active area, which was the smallest to its date [6].

In addition to graphene, the binary compound MoS$_2$, a member of the TMD family, displays interesting optical properties. Splendiani *et al.* showed that single-layer MoS$_2$ exhibits strong photoluminescence in contrast to the bulk form [7]. In addition, Mak *et al.* investigated monolayer and few-layer MoS$_2$ by optical spectroscopy and reported that compared to its bulk form, monolayer MoS$_2$ displays an increase in the quantum efficiency of luminescence by more than a factor of 10^4 [8,9]. Yin *et al.* indicated that a phototransistor based on monolayer MoS$_2$ yields better photoresponsivity than the graphene-based device [10]. Feng *et al.* studied the optical properties of monolayer MoS$_2$ with charged vacancies and found that vacancies induce extra peaks at low energy in the complex dielectric function [11].

The hexagonal structure of monolayer BN (*h*-BN), despite its structural similarity to graphene, is an insulator. It was

addressed that *h*-BN possesses an ultraviolet luminescent peak at 215 nm which is critical for deep-UV light-emitting and laser applications [12]. Furthermore, Kim *et al.* showed that 2D *h*-BN layers display very high transparency (transmittance over 99%) in the wavelength range of 250–900 nm, with a sharp absorption peak below 250 nm, where the optical gap was calculated as 6.07 eV [13]. Gao *et al.* indicated that the optical gap of *h*-BN increases with decreasing number of layers [14]. On the other hand, no cathodoluminescence or photoluminescence measurements of monolayer or few-layer *h*-BN structures have yet been reported. This indicates that further studies are needed in order to explore the optical properties of *h*-BN to expand its potential applications [15].

AlN is a III-V binary compound material with remarkable features which makes it very promising for advanced technological applications. It has high electrical resistivity [16,17] and high thermal conductivity [18]. As AlN has a wide direct electronic band gap of ∼6 eV [19], it can be potentially used in ultraviolet light emitting diodes (LEDs) and laser diodes [20–26]. At ambient conditions, the stable bulk form of AlN is wurtzite; however under high pressure, phase transitions from wurtzite to zinc blende or rocksalt forms were previously addressed [27–29]. Following the theoretical prediction [30], *h*-AlN was experimentally recently realized by Tsipas *et al.* [31]. Theoretical studies on nanofilms of AlN also indicate that the hexagonal phase (graphitic-like structure) is a lower energy configuration for only small thicknesses [32]. However, the domain of stable hexagonal structures can be extended to larger thicknesses by applying epitaxial strain [33].

Electronic properties of monolayer and few-layer forms of *h*-AlN were also theoretically studied [30,34] and excitonic effects on monolayer *h*-AlN were investigated [35]. However, to the best of our knowledge, there are no studies yet on the modification of the optoelectronic properties of monolayer and few-layer *h*-AlN, unlike the numerous experimental and theoretical works on well-known 2D materials such as graphene, *h*-BN, and MoS$_2$. Thus, the aim of the present study is to investigate the layer- and strain-dependent optical properties of the recently discovered *h*-AlN. An approach based on the random phase approximation on top of the

*durgun@unam.bilkent.edu.tr

density functional theory is adopted in order to depict the trends among the different cases, which is seen to be sufficient for a qualitative evaluation of the spectral optical quantities, considering also the computational burden that more advanced methodologies would bring. On the other hand, higher levels of accuracy in the calculations, namely the quasiparticle corrections and electron-hole interactions, are also accounted for in order to depict their influence on the optical features of specific cases.

The paper is organized as follows: In Sec. II, details of the computational methodology are presented, followed by a discussion of the results obtained from the four main aspects in Sec. III, (i) optical properties of bulk AlN crystal, (ii) layer- and (iii) strain-dependent optoelectronic properties of *h*-AlN, and (iv) many-body effects on the optical properties of monolayer and bilayer AlN. Our work is concluded in the final section.

II. COMPUTATIONAL METHODOLOGY

The ground-state properties of single- and multilayer *h*-AlN were investigated by performing first-principles calculations, using the projector augmented wave potentials (PAW) formalism [36] implemented in the Vienna *Ab initio* Simulation Package (VASP) [37–40] which is based on density functional theory (DFT). In order to describe the electron exchange and correlation, the Perdew-Burke-Ernzerhof (PBE) form of the generalized gradient approximation (GGA) was adopted [41,42]. The van der Waals interactions that have a significant role on layered materials were taken into account for the multilayered structures [43,44]. The energy cutoff of the plane-wave basis set was taken as 500 eV for all calculations. In order to minimize the total energy, the energy difference between the sequential steps was set to 10^{-5} eV. The allowed force on each atom and Gaussian smearing factor were taken as 0.05 eV/Å and 0.05 eV, respectively. A Gamma-centered $35 \times 35 \times 1$ mesh was used for Brillouin zone integrations for the primitive unit cell. To avoid spurious interactions between the periodic images, our calculations were performed with a supercell having ∼14 Å vacuum space. The details of atomic configurations of the bulk and multilayered structures of AlN can be found in Ref. [45].

Regarding the optical response calculations, the random phase approximation (RPA) [46,47] was undertaken on top of the DFT approach. A Monkhorst-Pack [48] *k*-point sampling of $127 \times 127 \times 1$ was adopted for PBE-RPA calculations of the 2D unit cell. A total number of 192 bands was used and the vacuum space was increased to 18 Å for the computation of the optical properties. The *k*-point mesh and number of bands were scaled accordingly for the bulk forms of both hexagonal and wurtzite AlN. Local field effects were accounted for both at the levels of Hartree and exchange-correlation potential.

Subsequently, hybrid functionals (HSE06) [49–51] and quasiparticle (QP) *GW* corrections [52–54] were undertaken in order to test the validity of the approaches, for specific cases (mono- and bilayer *h*-AlN). Finally, for the optical response beyond the independent-particle approach, the Bethe-Salpeter equation (BSE) [55–57] was employed on top of the G_0W_0 step, where the Tamm-Dancoff approximation (TDA) was adopted. Due to the computational burden, *k*-point sampling was limited to $19 \times 19 \times 1$ for the G_0W_0 approach. The

plane-wave cutoff was decreased to 350 eV and the basis set for the response functions was set to 240 eV for the many-body calculations. The total number of bands used for the *GW* calculations was increased to a maximum of 384. The excitonic effects were considered by undertaking the eight highest occupied valence bands and ten lowest unoccupied conduction bands.

Optical response functions presented in the upcoming discussions are expressed with the following relations. The calculated frequency-dependent complex dielectric function (*vide supra*) enables a variation of the linear optical spectral quantities such as the layer-dependent absorbance [$A(\omega)$], optical conductivity $\sigma(\omega)$, absorption coefficient $\alpha(\omega)$, and Fresnel reflectivity $R(\omega)$.

Layer-dependent absorbance is obtained from the imaginary dielectric function, as described below:

$$A(\omega) = \frac{\omega}{c} L \text{Im} \varepsilon(\omega), \tag{1}$$

where c is the speed of light and L is the total size of the cell in the layer-normal direction. The optical conductivity is given by the relation

$$\sigma(\omega) = \frac{\omega}{4\pi} \text{Im} \varepsilon(\omega). \tag{2}$$

The absorption coefficient is defined in the following way:

$$\alpha(\omega) = \sqrt{2} \omega \{ [\varepsilon_1(\omega)^2 + \varepsilon_2(\omega)^2]^{1/2} - \varepsilon_1(\omega) \}^{1/2}. \tag{3}$$

Frequency-dependent reflectivity at normal incidence is given by

$$R(\omega) = \left| \frac{\sqrt{\varepsilon(\omega)} - 1}{\sqrt{\varepsilon(\omega)} + 1} \right|^2, \tag{4}$$

where $\varepsilon(\omega)$ is the complex dielectric function.

III. RESULTS AND DISCUSSION

A. Optical properties of bulk AlN crystal

The frequency-dependent dielectric function of bulk AlN is calculated and compared with the experimental data in the literature [19,58]. The optical response of the hexagonal (*h*-) and wurtzite (*wz*-) forms of bulk AlN investigated at the level of DFT-RPA is shown in Fig. 1. The imaginary parts of the dielectric function [$\varepsilon_2(\omega)$] are denoted by the blue and green curves for the calculated and experimental data, respectively. For *h*-AlN, the main absorption peak of the calculated spectrum is situated around 8.6 eV, where the absorption phenomenon occurs the most intensely. The onset of interband absorption resides near 4.4 eV, which appears slightly higher than the direct band gap of 3.4 eV [45], where the difference most probably results from further band-to-band transitions with higher energy values. Another feature is the shoulder structure around both 6.8 eV and 7.3 eV. When compared, regarding the main peak position and the line shapes within the imaginary dielectric function, the spectrum predicted by DFT-RPA is generally in good agreement with the experimental data [58]. However, there is a 0.4 eV discrepancy between the onsets of absorption, as the experimental data indicate an absorption onset around 4.1 eV which could arise
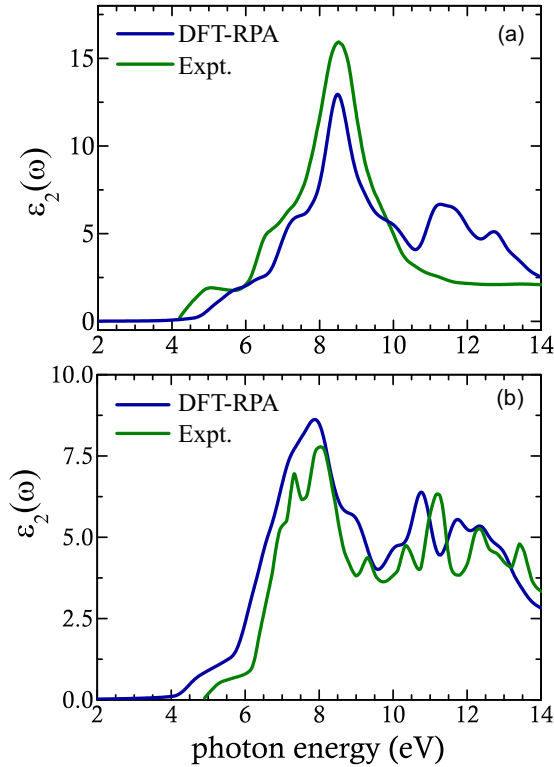
FIG. 1. (Color online) Optical absorption spectrum of (a) bulk hexagonal-AlN and (b) bulk wurtzite-AlN compared to experimentally obtained imaginary dielectric function [19,58].

from the noise in the experimental spectrum, since the plot does not reflect the most up-to-date measurement techniques.

In a similar manner, Fig. 1(b) displays $\varepsilon_2(\omega)$ of bulk wz-AlN. The onset of absorption is located around 4.2 eV, which is ∼0.8 eV lower than the experimental value [19]. This can be correlated with the underestimated band gap at the DFT-RPA level. The most significant feature is situated near 7.8 eV as a single peak, where the main peak splits into two for the experimental case. Above 10 eV, further peak features are observed for both spectra, with slight shifts from each other.

In summary, fair agreement with experimental data for both structures is indeed promising in the sense that despite the slight discrepancy within the absorption onset, the two plots match to a good extent especially regarding the most prominent peak of the spectrum. During the following discussion, for the sake of optimizing the computational expense, the results of layer- and strain-dependent optical response calculations are presented at the level of DFT-RPA, which is sufficient for qualitative comparisons. Nonetheless, for a more accurate description of the dielectric tensor, many-body effects play a significant role in determining the optical properties of 2D materials. Hence, they were employed for monolayer and bilayer h-AlN at the levels of quasiparticle G_0W_0 and excitonic effects within the solution of the Bethe-Salpeter equation. The results and comparisons can be found in the final section.

B. Layer-dependent optical properties of h-AlN

The results obtained from the investigation of the thickness-dependent optical properties of h-AlN up to four layers and
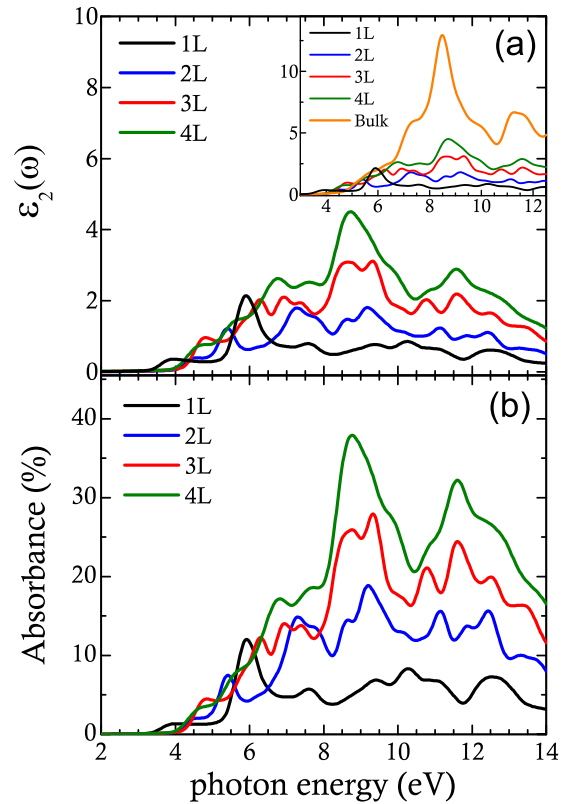

FIG. 2. (Color online) (a) Imaginary dielectric function and (b) layer-dependent absorbance spectra of single-layer, bilayer, three-layer, and four-layer (1L, 2L, 3L, and 4L) h-AlN. The comparison with bulk h-AlN crystal is shown as an inset.

the correlation with the electronic structure will be presented in this section. Theoretical analysis on AlN nanofilms also indicate that the hexagonal phase is favored energetically for small thicknesses (up to 12 layers) [32]. The optical responses of monolayer, bilayer, three-, and four-layer (1L, 2L, 3L, and 4L) h-AlN are analyzed by means of various optical spectra. To the best of our knowledge, related experimental data on the optical properties of single or few-layer h-AlN are not yet available in the literature; hence the results will be evaluated on the basis of theoretical calculations.

Although bulk h-AlN is a direct gap insulator, it was recently shown that its layered structure reveals an indirect gap character up to ten layers [45]. The differences in the band splittings of bulk and layered h-AlN were stressed previously, which implies that diversity in the optical spectra should also be expected. In Fig. 2, the $\varepsilon_2(\omega)$ and $A(\omega)$ of 1L, 2L, 3L, and 4L h-AlN are plotted in the same graph. Monolayer h-AlN's absorption spectrum is denoted by the black curve, which displays an onset at 3.4 eV. On the other hand, the onsets of 2L, 3L, and 4L AlN appear almost at the same values, around 4.2 eV. This result can be expected from their band structures (Fig. 3) since monolayer h-AlN reveals a band gap (E_g) of 2.91 eV, where a prominent direct transition is observed at the Γ point with an energy of 3.65 eV. On the other hand, 2L, 3L, and 4L h-AlN have E_g of ∼3.50 eV. This outcome is interesting as the layered structures except for monolayer act similarly and possess an onset closer to that of bulk h-AlN (4.5 eV).
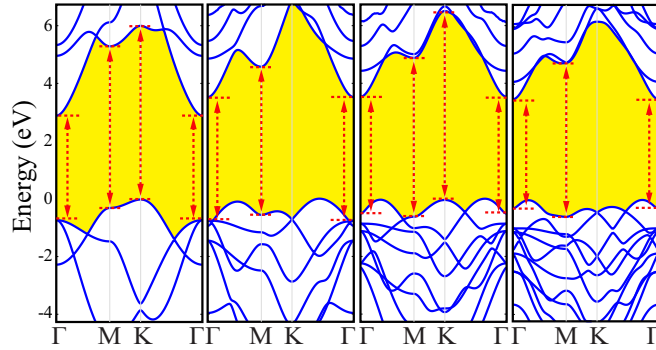
FIG. 3. (Color online) Electronic band structures of 1L, 2L, 3L, and 4L h-AlN. Zero level is set to the valence band maximum. Red arrows indicate important band-to-band (direct) transitions.

Moreover, 1L h-AlN exhibits a single distinct absorption peak around 6 eV, which is related to the important primary and secondary transitions at the Γ, M, and K points with transition energies in the range of 5.6 to 7.2 eV. On the other hand, 2L h-AlN (blue line) displays rather scattered multipeaks. The first one appears around 5.4 eV, the second near 7.2 eV, and the third one above 9.4 eV. Next, 3L h-AlN (red line) shows a relatively broadened absorption phenomenon, with steplike features, leading to multipeaks, occurring in the vicinity of 6.2 eV, 7.0 eV, and a broader peak centered at 9 eV. Finally, 4L h-AlN (green line) displays the similar steplike features in its absorption spectrum, with a relatively broadened plateau in between 6.6 and 8.2 eV, followed by a prominent absorption region with highest amplitude around 8.6 eV. It is observed that at higher energies (especially as of 8 eV), $\varepsilon_2(\omega)$ and absorbance spectra display gradually increasing intensities, with the increase in the number of layers. Layer-dependent absorbance [$A(\omega)$] which is shown in Fig. 2(b) reveals that the absorbance increases gradually once the layer number increases, reaching a maximum of 40% for four-layered h-AlN, where this is much lower for the monolayer case. As can be deduced from the band structures of layered systems, the extra peaks of interband absorption come into play with contribution of additional layers. Moreover, when the optical spectrum of 4L h-AlN is compared to the one of bulk h-AlN which is shown as an inset of Fig. 2(a), it is observed that they display similar features especially in between 5.2 and 6.8 eV. However an intense absorption occurs for bulk h-AlN in the range of 6.8–10.8 eV, with much higher amplitude with respect to the 4L h-AlN indicating that more layers are required to attain a bulklike character.

Once the frequency-dependent complex dielectric tensor is calculated, it is possible to obtain and compare various optical properties. Accordingly, the optical conductivity [Im$\sigma(\omega)$], absorption coefficient [$\alpha(\omega)$], and reflectivity spectra [$R(\omega)$] of 1L, 2L, 3L, and 4L h-AlN are calculated as a function of photon energy, $\hbar\omega$, and are exhibited in Fig. 4. The former two graphs display, similarly to the $\varepsilon_2(\omega)$, that the rather substantial absorption is restricted to a range between 4 eV to above 10 eV, predominantly in the region above 8 eV, for all the systems of concern. Evidently, the peak intensities related to 4L h-AlN are the strongest, due to the well-distinguished broad peak around 9 eV. As for the frequency-dependent reflectivity function,
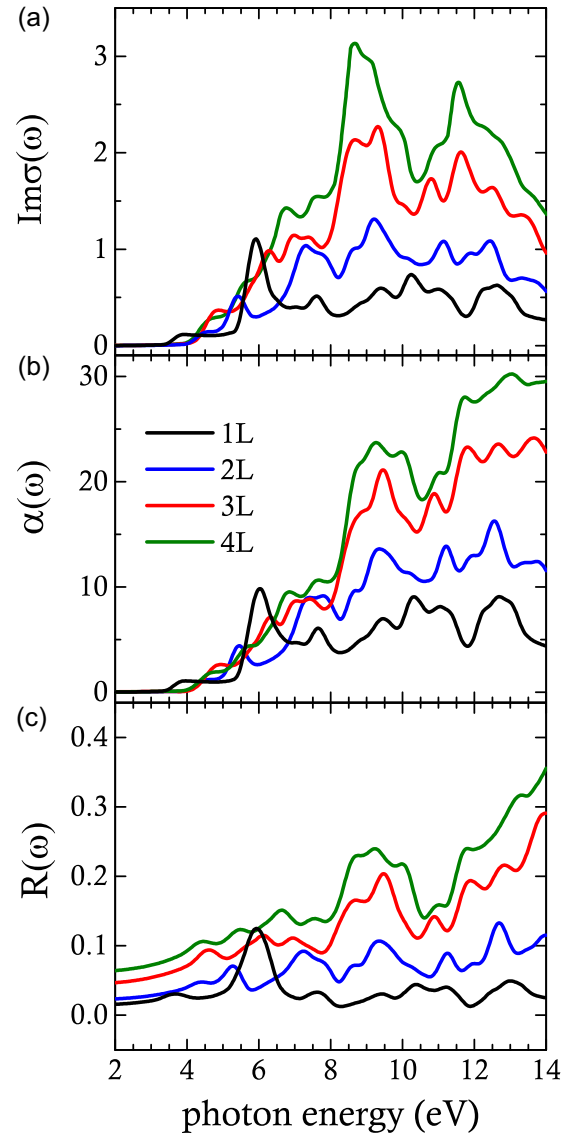

FIG. 4. (Color online) (a) Frequency-dependent optical conductivity, (b) absorption coefficient, and (c) reflectivity of 1L, 2L, 3L, and 4L h-AlN as a function of $\hbar\omega$.

for all the systems, it is observed that the reflectance over the visible range and slightly above is generally quite small, which points to a potentially transparent material.

Pointing to prominent optical absorption over the UV range, layered h-AlN is also a promising material for optoelectronic applications. Considered as a significant input for potential nano-optoelectronic devices to be composed of layered h-AlN, the effective mass values for electron (m_e^*) and hole (m_h^*) are also calculated. The layer-dependent m_e^* and m_h^* are presented in Fig. 5. To obtain m^*, we fit the valence band maximum and conduction band minimum to a parabola, where the inverse of the second-order term's coefficient, multiplied by a factor, is considered as the m_e^* and m_h^*, respectively. Our results indicate that for 1L, m_e^* is equal to 0.50 m_0 and decreases slowly as the number of layers increases and converges to the bulk value. On the other hand, m_h^* is calculated to be 1.53 m_0 for the monolayer case and decreases dramatically upon increasing the number of layers. It could be informative
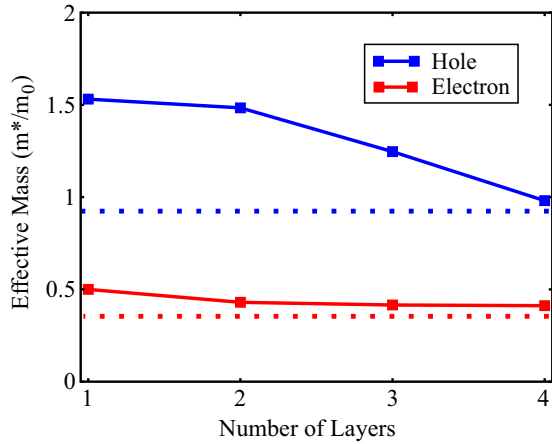
FIG. 5. (Color online) The variation of electron (red line) and hole effective mass (blue line) with respect to the number of layers. The bulk values are shown by dashed lines.

to make a comparison with some other 2D semiconducting systems. When only the monolayer case is considered m_e^* is comparable to that of layered BN [59] ($m_e^* = m_h^* = 0.54$ m_0) and monolayer MoS$_2$ [60] ($m_e^* = 0.37$–0.38 m_0 and $m_h^* = 0.44$–0.48 m_0). However, m_h^* is significantly higher than both monolayer BN and MoS$_2$. The range and variation of effective mass and electronic band gap suggest that layered h-AlN is a promising candidate material for next-generation electronic devices.

Finally, the effect of spin-orbit (SO) coupling on the optoelectronic properties should be considered too, since it can be significant for 2D systems. For instance, despite the 1 meV SO splitting in silicene [61], the SO splitting of germanene is calculated to be 23 meV [62]. In this sense, SO coupling was also taken into account in our calculations. The SO splitting is calculated to be 8 meV for monolayer h-AlN. Its effect on the optical properties was found to be negligible, based on an evaluation of the $\varepsilon_2(\omega)$ of monolayer h-AlN.

C. Strain-dependent optical properties of h-AlN

In addition to the layer-dependence, the optical properties of monolayer h-AlN are also investigated under the influence of biaxial tensile strain. Theoretical studies on nanofilms of AlN (and also other wurtzite materials) reveals that the thickness
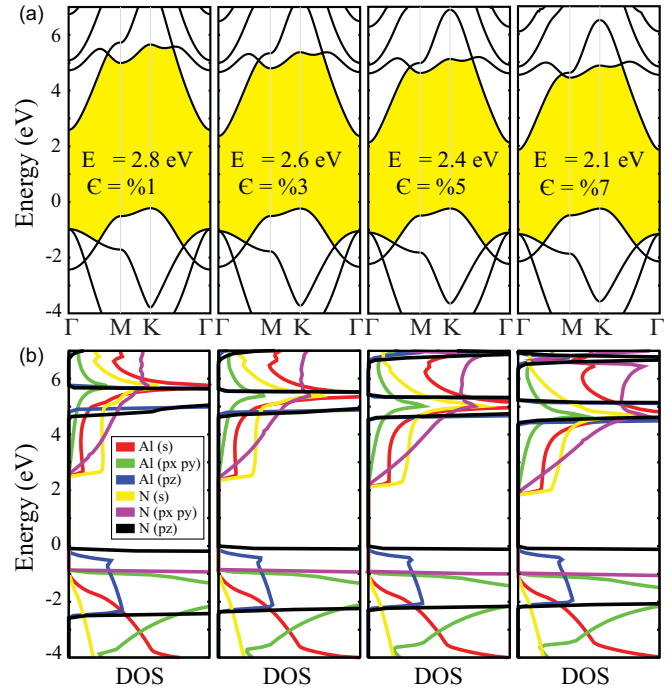

FIG. 7. (Color online) (a) Strain-dependent band structures indicating the variation of the band gap values (E) as a function of strain (ϵ) and (b) partial densities of states of monolayer h-AlN.

range of the stable hexagonal phase depends on strain and can be extended to thicker films by epitaxial tensile strain [33]. We apply strain at values of 1%, 3%, 5%, and 7% since higher stress values can induce instability and are also very difficult to achieve for practical applications, hence are not considered here. Strain can be caused by loading or the underlying substrate, and is a relevant phenomenon for 2D materials due to the rather large tensile strain obtained experimentally. The variation of $\varepsilon_2(\omega)$ of monolayer h-AlN with strain is shown in Fig. 6(a). The first observation reveals that the spectra are globally shifted toward lower photon energies, in a general manner. The gradual shift is almost uniform and increases with the amount of applied strain. In order to understand the origin of the shift and relate with the electronic structure, we also calculated the strain-dependent band structure of monolayer h-AlN (Fig. 7). Biaxial strain is naturally expected to alter the electronic properties. More precisely, increasing or decreasing
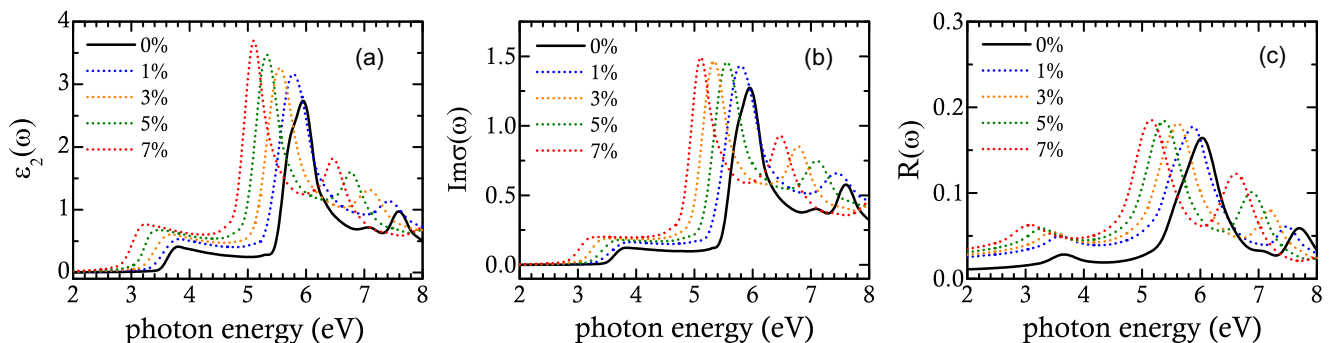

FIG. 6. (Color online) (a) Imaginary dielectric function, (b) absorption coefficient, and (c) frequency-dependent reflectivity of single-layer h-AlN under strain. Black solid curve stands for the unstrained case and dashed lines for strain values of 1%, 3%, 5%, and 7%, respectively.

TABLE I. Optimized lattice constant, band gap, absorption onset, and absorption peak position values of strained h-AlN.

	Lattice constant (Å)	Band gap (eV)	Onset I (eV)	Onset II (eV)	PL peak (eV)
Unstrained	3.13	2.91	3.45	5.45	5.93
1%	3.16	2.8	3.32	5.23	5.82
3%	3.22	2.6	3.22	5.10	5.54
5%	3.28	2.4	3.05	4.89	5.32
7%	3.44	2.1	2.80	4.70	5.10

the bond length as well as confinement effects can modify the electronic structure. Our analysis indicates that the E_g values are also reduced monotonically as the strain value is increased. The decrease in E_g can be attributed to the modification of orbitals under strain. Partial density of states analysis shows that except for the p_z orbital of Al and N atoms, with increasing strain, the orbitals and the corresponding bands are placed at lower energy both in the valence and conduction bands. More explicitly, the energies of s and p_{xy} orbitals decrease relative to p_z orbitals which is plausible since the s and p_{xy} orbitals are effected by confinement in the direction of strain. On the other hand, the p_z orbitals which are out of plane of the structure are influenced very little. Therefore, the decrease in E_g values under strain can be explained by the difference between in-plane and out-of-plane orbitals.

Next, we analyze the change in the optical spectra quantitatively via a global joint density of states like spectrum [obtained as $\varepsilon_2(\omega)^2 \times$ photon energy]. The three quantities yielded by this analysis are the absorption onsets ("onset I" in Table I indicates the first steplike increase in the spectrum, and "onset II" refers to the value at which the prominent absorption peak kicks off) and the main peak position.

Regarding the absorption onset values, onset I varies from 3.45 to 2.80 eV, upon being subjected to tensile strain. The average difference among the onset values comes out as 0.16 eV. Next, it is seen that onset II varies from 5.45 to 4.70 eV, pointing to an average shift of 0.18 eV. Both shifts are toward lower photon energies. The third feature to be discussed in Fig. 6(a) and Table I is the main absorption peak's position, which is redshifted by approximately 0.24 eV from 1% to 7% strain. The feature most affected by the applied strain is the peak position, followed by the onset values. It is no surprise that in-plane tensile strain tunes the optical properties in such a way that the absorption spectrum is regularly (globally) redshifted as shown in Figs. 6(b) and 6(c), well known for electronic properties and also from some recent work on the optical properties of 2D materials [63]. In conclusion, the optical spectra of 2D monolayer h-AlN are also quite sensitive to biaxial tensile strain, as well as its electronic properties, which is promising for the potential optoelectronic applications by strain engineering.

D. Many-body calculations of the optical properties of monolayer and bilayer h-AlN

As the prominence of many-body effects in the excited-state properties of band gap materials is well known, the optical absorption spectra of specific cases, monolayer and bilayer h-AlN, were also calculated at higher levels of accuracy. The hybrid functionals and non-self-consistent quasiparticle G_0W_0

within RPA were used. The electron-hole (e-h) interactions are taken into account by solving the BSE, details of which are given in the methodology part. The results of the comparison between the different methods and number of layers are shown in Fig. 8. As seen in the upper panel (a), the spectrum of single-layer h-AlN given by the HSE-RPA calculation (orange plot) is globally shifted towards higher frequencies by nearly 1 eV with respect to its PBE-RPA counterpart (black plot). Likewise, the absorption onset value is higher than that of PBE by slightly above 1 eV. The absorption peak position given by HSE appears around 7 eV, which is not surprising since the correction of band gap by hybrid functionals, thus the optical gap, is a common trend. As exhibited by the red plot, the single-shot G_0W_0 yields a further blueshifted optical response, with a main peak residing around 8 eV. Regarding both the absorption onset (slightly below 5.5 eV) and peak
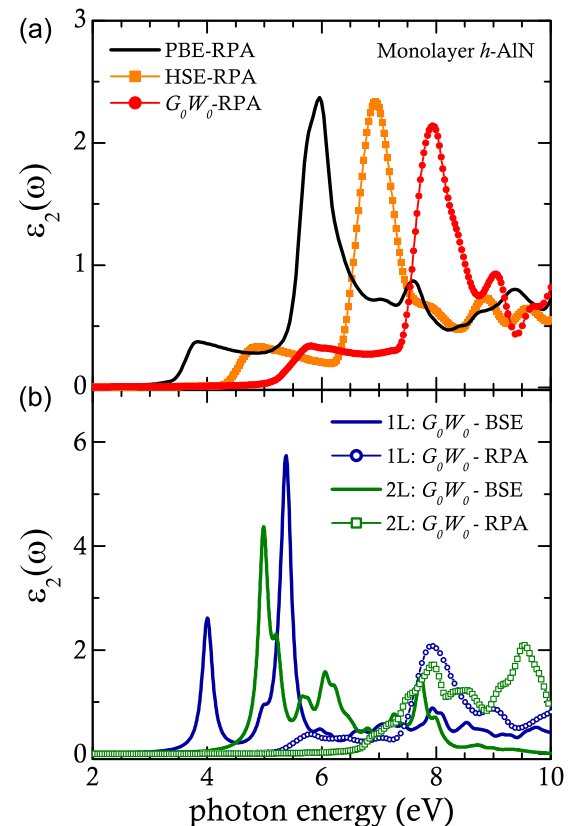

FIG. 8. (Color online) Many-body calculations of the optical response of monolayer and bilayer h-AlN. (a) Comparison of RPA spectra based on PBE, HSE, and G_0W_0 calculations for monolayer h-AlN and (b) optical spectra of mono- and bilayer h-AlN with electron-hole interactions taken into account.

positions, the G_0W_0 method reveals a global blueshift with respect to PBE- and HSE-RPA spectra.

The absorption spectra of monolayer (blue plot) and bilayer (green plot) structures given by single-shot G_0W_0-BSE calculation are displayed in the lower panel (b) of Fig. 8. Accordingly, for single-layer h-AlN, two sharp peaks are located at 4.0 and 5.38 eV (also a small shoulder at 5 eV), the former being closer to the optically active region. The optical transitions below the G_0W_0 optical gap (green plot with squares) indicate a resonant light-matter coupling present in monolayer AlN with wide electronic gap, arising from the excitonic transitions. Similarly, the BSE spectrum of bilayer AlN displays a major peak at nearly 5 eV and a second nonsharp feature around 6 eV, both below the band gap yielded by G_0W_0. Hence, the optical features for both structures are substantially dominated by the excitonic effects, pointing to strongly bound excitons, due to the e-h interactions stemming from weak screening in wide-gap low-dimensional AlN. We calculate the exciton binding energy for monolayer AlN as $\sim$1.7 eV. This optically active exciton corresponds to the first peak located at 4.0 eV [35]. For bilayer h-AlN, binding energy increases and becomes nearly 2.2 eV, as the band gap is opened up compared to the monolayer case. For the sake of comparison with other 2D materials with significant band gaps, the binding energies are revealed as $\sim$0.8 eV [64], $\sim$1 eV [65], and $\sim$2.1 eV [66] for monolayer phosphorene, MoS_2, and BN, respectively. Moreover, the exciton binding energy of layered AlN is substantially higher than that of its wurtzite structure (80 meV) [19] and AlN films (63 meV) [67]. Evidently, the strongly bound excitons underline that for layered h-AlN, e-h effects can be significant to enhance the optical features in the absorption spectrum.

IV. CONCLUSIONS

In conclusion, we examined in detail the layer- and strain-dependent optoelectronic properties of h-AlN starting from its bulk crystal form. We calculated the layer-dependent absorbance, optical conductivity, absorption coefficient, and frequency-dependent reflectivity and investigated their variation with the increasing number of layers. The absorbance was found to increase when more layers were considered. In general, prominent optical absorption was observed to occur within the UV range, promising for optoelectronic applications aimed for the ultraviolet spectral region. Hence, the layered forms of h-AlN are expected to display rather transparent features in the visible-light range. Furthermore, our results indicated that the absorption spectrum is globally redshifted under the applied strain. The electronic properties of layered h-AlN were also computed in order to clarify their relation with the optical spectra. The band gaps, similarly to the interband absorption onsets, were found to vary with the increasing number of layers and amount of strain. While the many-body corrections to the optical response calculations of h-AlN induced blueshifted spectra in general, evidence of bound excitons was also found for the layered structures of AlN. In summary, it was shown that the optoelectronic properties of layered h-AlN can be controlled and tuned by modifying their structure and applying strain. Since extensive knowledge of the optical properties of layered AlN is prominent for future device applications, the theoretical findings in this paper can further enlighten investigations focusing on the design of optoelectronic devices made of 2D h-AlN.

[1] K. S. Novoselov, A. K. Geim, S. V. Morozov, D. Jiang, Y. Zhang, S. V. Dubonos, I. V. Grigorieva, and A. A. Firsov, Science **306**, 666 (2004).

[2] R. R. Nair, P. Blake, A. N. Grigorenko, K. S. Novoselov, T. J. Booth, T. Stauber, N. M. R. Peres, and A. K. Geim, Science **320**, 1308 (2008).

[3] C. Casiraghi, A. Hartschuh, E. Lidorikis, H. Qian, H. Harutyunyan, T. Gokus, K. S. Novoselov, and A. C. Ferrari, Nano Lett. **7**, 2711 (2007).

[4] T. Gokus, R. R. Nair, A. Bonetti, M. Böhmler, A. Lombardo, K. S. Novoselov, A. K. Geim, A. C. Ferrari, and A. Hartschuh, ACS Nano **3**, 3963 (2009).

[5] K. F. Mak, J. Shan, and T. F. Heinz, Phys. Rev. Lett. **104**, 176404 (2010).

[6] M. Liu, X. Yin, E. Ulin-Avila, B. Geng, T. Zentgraf, L. Ju, F. Wang, and X. Zhangz, Nature (London) **474**, 64 (2011).

[7] A. Splendiani, L. Sun, Y. Zhang, T. Li, J. Kim, C.-Y. Chim, G. Galli, and F. Wang, Nano Lett. **10**, 1271 (2010).

[8] K. F. Mak, C. Lee, J. Hone, J. Shan, and T. F. Heinz, Phys. Rev. Lett. **105**, 136805 (2010).

[9] G. Eda, H. Yamaguchi, D. Voiry, T. Fujita, M. Chen, and M. Chhowalla, Nano Lett. **11**, 5111 (2011).

[10] J. Z. Yin, H. Li, H. Li, L. Jiang, Y. Shi, Y. Sun, G. Lu, Q. Zhang, X. Chen, and H. Zhang, ACS Nano **6**, 74 (2012).

[11] L.-p. Feng, J. Su, and Z.-t. Liu, J. Alloys Compd. **613**, 122 (2014).

[12] K. Watanabe, T. Taniguchi, and H. Kanda, Nat. Mater. **3**, 404 (2004).

[13] K. Kim, A. Hsu, X. Jia, S. M. Kim, Y. Shi, M. Hofmann, D. Nezich, J. F. Rodriguez-Nieva, M. Dresselhaus, T. Palacios, and J. Kong, Nano Lett. **12**, 161 (2011).

[14] Y. Gao, W. Ren, T. Ma, Z. Liu, Y. Zhang, W. B. Liu, L. P. Ma, X. Ma, and H. M. Cheng, ACS Nano **7**, 5199 (2013).

[15] X. Song, J. Hu, and H. Zeng, J. Mater. Chem. C **1**, 2952 (2013).

[16] A. V. Virkar, T. B. Jackson, and R. A. Cutler, J. Am. Ceram. Soc. **72**, 2031 (1989).

[17] A. W. Weimer, G. A. Cochran, G. A. Eisman, J. P. Henley, B. D. Hook, L. K. Mills, T. A. Guiton, A. K. Knudsen, N. R. Nicholas, J. E. Volmering, and W. G. Moor, J. Am. Ceram. Soc. **77**, 3 (1994).

[18] G. A. Slack, R. A. Tanzilli, R. O. Pohl, and J. W. Vandersande, J. Phys. Chem. Solids **48**, 641 (1987).

[19] J. Li, K. B. Nam, M. L. Nakarmi, J. Y. Lin, H. X. Jiang, Pierre Carrier, and Su-Huai Wei, Appl. Phys. Lett. **83**, 5163 (2003).

[20] I. Akasaki and H. Amano, Jpn. J. Appl. Phys. **36**, 5393 (1997).

[21] F. A. Ponce and D. P. Bour, Nature (London) **386**, 351 (1997).

[22] J. Han, M. H. Crawford, R. J. Shul, J. J. Figiel, M. Banas, L. Zhang, Y. K. Song, H. Zhou, and A. V. Nurmikko, Appl. Phys. Lett. **73**, 1688 (1998).

[23] T. Nishida and N. Kobayashi, Phys. Status Solidi A **176**, 45 (1999).

[24] V. Adivarahan, W. H. Sun, A. Chitnis, M. Shatalov, S. Wu, H. P. Maruska, and M. A. Khan, Appl. Phys. Lett. **85**, 2175 (2004).

[25] H. Hirayama, J. Appl. Phys. **97**, 091101 (2005).

[26] A. Khan, K. Balakrishnan, and T. Katona, Nat. Photonics **2**, 77 (2008).

[27] L. Hultman, S. Benhenda, G. Radnoczi, J.-E. Sundgren, J. E. Greene, and I. Petrov, Thin Solid Films **215**, 152 (1992).

[28] M. Ueno, A. Onodera, O. Shimomura, and K. Takemura, Phys. Rev. B **45**, 10123 (1992).

[29] Q. Xia, H. Xia, and A. L. Ruoff, J. Appl. Phys. **73**, 8198 (1993).

[30] H. Sahin, S. Cahangirov, M. Topsakal, E. Bekaroglu, E. Akturk, R. T. Senger, and S. Ciraci, Phys. Rev. B **80**, 155453 (2009).

[31] P. Tsipas, S. Kassavetis, D. Tsoutsou, E. Xenogiannopoulou, E. Golias, S. A. Giamini, C. Grazianetti, D. Chiappe, A. Molle, M. Fanciulli, and A. Dimoulas, Appl. Phys. Lett. **103**, 251605 (2013).

[32] C. L. Freeman, F. Claeyssens, N. L. Allan, and J. H. Harding, Phys. Rev. Lett. **96**, 066102 (2006).

[33] D. Wu, M. G. Lagally, and F. Liu, Phys. Rev. Lett. **107**, 236101 (2011).

[34] H. L. Zhuang, A. K. Singh, and R. G. Hennig, Phys. Rev. B **87**, 165415 (2013).

[35] D. V. Fakhrabad, N. Shahtahmasebi, and M. Ashhadi, Superlattices Microstruct. **79**, 38 (2015).

[36] M. Gajdos, K. Hummer, G. Kresse, J. Furthmüller, and F. Bechstedt, Phys. Rev. B **73**, 045112 (2006).

[37] G. Kresse and J. Hafner, Phys. Rev. B **47**, 558 (1993).

[38] G. Kresse and J. Hafner, Phys. Rev. B **49**, 14251 (1994).

[39] G. Kresse and J. Furthmüller, Comput. Mater. Sci. **6**, 15 (1996).

[40] G. Kresse and J. Furthmüller, Phys. Rev. B **54**, 11169 (1996).

[41] J. P. Perdew, K. Burke, and M. Ernzerhof, Phys. Rev. Lett. **77**, 3865 (1996).

[42] J. P. Perdew, K. Burke, and M. Ernzerhof, Phys. Rev. Lett. **78**, 1396 (1997).

[43] S. J. Grimme, Comput. Chem. **27**, 1787 (2006).

[44] T. Bucko, J. Hafner, S. Lebegue, and J. G. Angyan, J. Phys. Chem. A **114**, 11814 (2010).

[45] C. Bacaksiz, H. Sahin, H. D. Ozaydin, S. Horzum, R. T. Senger, and F. M. Peeters, Phys. Rev. B **91**, 085430 (2015).

[46] D. Bohm and D. Pines, Phys. Rev. **82**, 625 (1951); **85**, 338 (1952); **92**, 609 (1953).

[47] H. Ehrenreich and M. H. Cohen, Phys. Rev. **115**, 786 (1959).

[48] H. J. Monkhorst and J. D. Pack, Phys. Rev. B **13**, 5188 (1976).

[49] J. Paier, M. Marsman, K. Hummer, G. Kresse, I. C. Gerber, and J. G. Angyan, J. Chem. Phys. **124**, 154709 (2006).

[50] J. Heyd, G. E. Scuseria, and M. Ernzerhof, J. Chem. Phys. **118**, 8207 (2003); **124**, 219906 (2006).

[51] J. Heyd and G. E. Scuseria, J. Chem. Phys. **120**, 7274 (2004); **121**, 1187 (2004).

[52] L. Hedin, Phys. Rev. **139**, A796 (1965).

[53] M. S. Hybertsen and S. G. Louie, Phys. Rev. B **34**, 5390 (1986).

[54] M. Shishkin and G. Kresse, Phys. Rev. B **74**, 035101 (2006).

[55] E. E. Salpeter and H. A. Bethe, Phys. Rev. **84**, 1232 (1951).

[56] M. Rohlfing and S. G. Louie, Phys. Rev. B **62**, 4927 (2000).

[57] G. Onida, L. Reining, and A. Rubio, Rev. Mod. Phys. **74**, 601 (2002).

[58] S. Loughin, R. H. French, W. Y. Ching, Y. N. Xu, and G. A. Slack, Appl. Phys. Lett. **63**, 1182 (1993).

[59] X. Cao, B. Clubine, J. Edgar, J. Lin, and H. Jiang, Appl. Phys. Lett. **103**, 191106 (2013).

[60] H. Peelaers and C. G. Van de Walle, Phys. Rev. B **86**, 241401 (2012).

[61] C. C. Liu, H. Jiang, and Y. Yao, Phys. Rev. B. **84**, 195430 (2011).

[62] V. O. Ozcelik, E. Durgun, and S. Ciraci, J. Phys. Chem. Lett. **5**, 2694 (2014).

[63] H. Shi, H. Pan, Y.-W. Zhang, and B. I. Yakobson, Phys. Rev. B **87**, 155304 (2013).

[64] V. Tran, R. Soklaski, Y. Liang, and L. Yang, Phys. Rev. B **89**, 235319 (2014).

[65] D. Y. Qiu, F. H. da Jornada, and S. G. Louie, Phys. Rev. Lett. **111**, 216805 (2013).

[66] L. Wirtz, A. Marini, and A. Rubio, Phys. Rev. Lett. **96**, 126104 (2006).

[67] E. Silveira, J. A. Freitas Jr., M. Kneissl, D. W. Treat, N. M. Johnson, G. A. Slack, and L. J. Schowalter, Appl. Phys. Lett. **84**, 18 (2004).